

Imprints of the Local Bubble and Dust Complexity on Polarized Dust Emission

GEORGE HALAL ^{1,2}, S. E. CLARK ^{1,2} AND MEHRNOOSH TAHANI ^{1,2,3}

¹*Department of Physics, Stanford University, Stanford, CA 94305, USA*

²*Kavli Institute for Particle Astrophysics and Cosmology, Stanford, CA 94305, USA*

³*Banting and KIPAC Fellow, Stanford, CA 94305, USA*

ABSTRACT

Using 3D dust maps and Planck polarized dust emission data, we investigate the influence of the 3D geometry of the nearby interstellar medium (ISM) on the statistics of the dust polarization on large (80') scales. We test the idea that the magnetic field in the nearby dust is preferentially tangential to the Local Bubble wall, but we do not find an imprint of the Local Bubble geometry on the dust polarization fraction. We also test the hypothesis that the complexity of the 3D dust distribution drives some of the measured variation of the dust polarization fraction. We compare sightlines with similar total column densities and find evidence that, on average, the dust polarization fraction decreases when the dust column is substantially distributed among multiple components at different distances. Conversely, the polarization fraction is higher for sightlines where the dust is more concentrated in 3D space. This finding is statistically significant for the dust within 1.25 kpc, but the effect disappears if we only consider dust within 270 pc. The extended 3D dust distribution, rather than solely the dust associated with the Local Bubble, plays a role in determining the observed dust polarization fraction on these scales. This conclusion is consistent with a simple analytical prediction and remains robust under various modifications to the analysis. These results illuminate the relationship between the 3D geometry of the ISM and tracers of the interstellar magnetic field. We also discuss implications for our understanding of the polarized dust foreground to the cosmic microwave background.

Keywords: Interstellar dust (836) — Cosmic microwave background radiation (322) — Algorithms (1883) — Interstellar magnetic fields (845) — Interstellar medium (847) — Galaxy magnetic fields (604) — Milky Way magnetic fields (1057) — Magnetic fields (994) — Superbubbles (1656) — Interstellar reddening (853) — Interstellar dust extinction (837) — Extinction (505)

1. INTRODUCTION

Interstellar magnetic fields play an important role in various astrophysical processes (see, e.g., Ferrière 2001; Heiles & Haverkorn 2012; Pattle et al. 2023). However, little is known about the magnetic field structure in the nearby interstellar medium (ISM). Some work has suggested connections between the local magnetic field structure and other tracers of ISM morphology, perhaps due to dynamical influences, e.g. the formation of structures like superbubbles (e.g., Santos et al. 2011; Frisch et al. 2012; Berdyugin et al. 2014; Tahani et al. 2022a,b).

Aspherical dust grains in the ISM emit photons with an electric field oriented preferentially along their long axes (Purcell 1975). The short axes of typical dust grains are preferentially aligned with the local magnetic field orientation (Andersson et al. 2015). As a result, their thermal emission is partially polarized perpendicular to the orientation of the magnetic field. Therefore, measurements of the polarized dust emission are used as a probe for the plane-of-sky magnetic field orientation in dusty regions of the ISM.

Recent evidence suggests that variations in the dust polarization fraction over large angular scales in the diffuse sky are mainly driven by the structure of the magnetic field. Planck Collaboration et al. (2020a) probed the influence of the magnetic field geometry on the dust polarization fraction by comparing the local polarization

angle dispersion with the 353 GHz polarization fraction. They calculated the polarization angle dispersion for an annulus with inner and outer radii of 40' and 120', and found that the 353 GHz polarization fraction is anti-correlated with the local polarization angle dispersion at 160' resolution. They showed that this relationship is consistent with models that only include topological effects of the turbulent magnetic field, but otherwise have uniform dust properties and alignment. [Planck Collaboration et al. \(2020a\)](#) conclude that the polarization fraction and the dispersion of polarization angles are similarly sensitive to the structure of the magnetic field. [Hensley et al. \(2019\)](#) further showed that some of the variability in the dispersion of polarization angles, and thus the polarization fraction, can be explained by the magnetic inclination angle, i.e., the angle between the magnetic field and the plane of the sky. The polarization fraction is maximized when the magnetic field is tangential to the plane of the sky and zero when it is parallel to the line of sight. [Chen et al. \(2019\)](#) and [Sullivan et al. \(2021\)](#) used statistical properties of the observed polarization fraction to estimate the average inclination angle of molecular cloud-scale magnetic fields.

The observed dust polarization fraction also depends on other factors, such as the dust grain alignment efficiency ([King et al. 2019](#); [Medan & Andersson 2019](#)), the phase distribution of the neutral interstellar medium ([Lei & Clark 2023](#)), and measurement noise. However, the 3D structure of the magnetic field is one of the major factors ([Clark 2018](#); [Hensley et al. 2019](#); [Planck Collaboration et al. 2020a](#)).

This paper focuses on latitudes and angular scales where we expect that the dust polarization primarily traces the nearby dust. Our Sun's current location is near the center of a superbubble, which is thought to have been created by supernova explosions within the past $10\text{-}15 \times 10^6$ years ([Cox & Reynolds 1987](#); [Maíz-Apellániz 2001](#); [Breitschwerdt et al. 2016](#)). It is commonly known as the Local Bubble, Local Cavity, or Local Chimney ([Welsh et al. 2004](#); [Puspitarini & Lallement 2012](#)). Since star formation tends to be concentrated, sequential supernovae are common ([Zucker et al. 2022](#); [Watkins et al. 2023](#); [Barnes et al. 2023](#); [Sandstrom et al. 2023](#)). Supernova explosions sweep up matter and magnetic field lines, leaving behind low-density superbubbles on the order of hundreds of parsecs in diameter ([Kim & Ostriker 2015](#)). The swept-up matter is compressed into a shell surrounding the expanding superbubble, which is thought to trigger the formation of dense gas and stars ([Elmegreen 2011](#); [Dawson 2013](#); [Inutsuka et al. 2015](#)).

It is reasonable to expect that the formation of the Local Bubble dramatically influenced the magnetic field

geometry in the nearby ISM. Some studies have aimed at modeling the geometry of the wall of cold neutral gas and dust surrounding the Local Bubble (e.g., [Alves et al. 2018](#); [Pelgrims et al. 2020](#)). Since the geometry of the magnetic field affects the measured polarization fraction, we search for an imprint of the Local Bubble geometry on the dust polarization fraction in this paper.

Additionally, one of the probes of the 3D spatial distribution of the neutral ISM is dust extinction toward stars. This is due to the scattering and absorption of starlight by dust. The extinction of a star's apparent magnitude is correlated with the dust column density along the line of sight from the observer to that star. The Gaia survey provided accurate distances to more than a billion stars within a few kiloparsecs from the Sun. Combining this distance information with the level of extinction towards each star has been transformative for the construction of 3D maps of the differential dust extinction ([Lallement et al. 2019](#); [Leike et al. 2020](#); [Vergely et al. 2022](#); [Edenhofer et al. 2023](#)). We use several 3D dust maps to quantify the complexity of the spatial distribution of the dust along the line of sight. We use that to explore the relationship between the 3D dust distribution and the measured polarization fraction.

In this work, we investigate the relationship between the 3D geometry of the nearby ISM and the dust polarization fraction. We start by introducing the data we use in Section 2. In Section 3, we search for an imprint of the Local Bubble geometry on the dust polarization fraction. In Section 4, we test how the polarization fraction is affected by the line-of-sight complexity of the dust. We discuss the implications of our results and conclude in Section 5.

2. DATA

2.1. *Planck Data Products*

We use the 80' R3.00 Planck data processed with the Generalized Needlet Internal Linear Combination (GNILC; [Remazeilles et al. 2011](#)) method at 353 GHz to remove the Cosmic Infrared Background (CIB) radiation from the Galactic dust emission ([Planck Collaboration et al. 2016a](#)). Following the fiducial offset corrections adopted by the Planck collaboration, we subtract $452 \mu\text{K}_{\text{CMB}}$ from the GNILC total intensity map to correct for the CIB monopole then add a Galactic offset correction of $63 \mu\text{K}_{\text{CMB}}$ ([Planck Collaboration et al. 2020a](#)). Because the GNILC data are at FWHM= 80', we downgrade the maps from their native HEALPix pixelization ([Górski et al. 2005](#)) at $N_{\text{side}} = 2048$ to $N_{\text{side}} = 64$. We also use the R3.01 Planck data at 353 GHz, smoothed to 80' as a cross-check ([Planck Collaboration et al. 2020b](#)). All of these maps use the

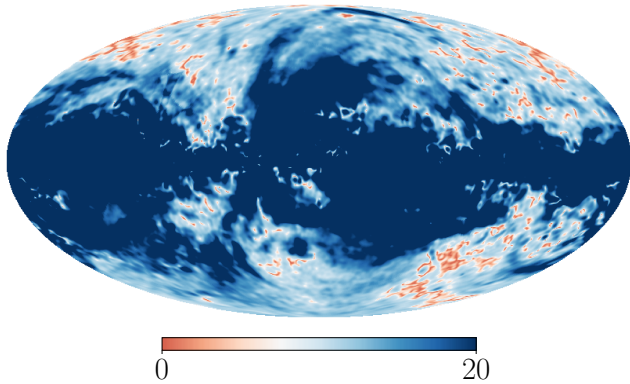


Figure 1. A map of the debiased signal-to-noise ratio of the Planck GNILC polarization fraction at $80'$. This is plotted with a diverging linear colorbar centered on 3, the cutoff we use as part of our sightline selections in Sections 3 and 4, with the allowed regions shown in blue.

COSMO polarization convention. We do not convert to the IAU polarization convention.

We use the modified asymptotic estimator of Plaszczyński et al. (2014) to debias the polarized intensity of the GNILC dust emission map and the associated uncertainty. We obtain a signal-to-noise ratio map of the polarization fraction, SNR_p , shown in Figure 1.

We estimate the total dust extinction over the full sky using Planck data products. Planck Collaboration et al. (2014) and Planck Collaboration et al. (2016a) fit a modified blackbody spectrum to the GNILC dust maps at different frequencies to estimate the dust temperature, spectral index, and optical depth over the sky. The dust optical depth is correlated with the reddening of quasars (Planck Collaboration et al. 2014). Using this observation, Planck Collaboration et al. (2016a) multiply the GNILC dust optical depth map by a factor of 1.49×10^{-4} mag to construct a GNILC $E(B - V)$ map. We query the publicly available `dustmaps` Python package (Green 2018) for the Planck Collaboration et al. (2016a) GNILC $E(B - V)$ map. Assuming a standard extinction law, we multiply the GNILC $E(B - V)$ map by 3.1 to obtain A_V^{Planck} .

2.2. 3D Dust Maps and Local Bubble Geometries

In Section 3, we use the 3D model of the Local Bubble surface geometry constructed by Pelgrims et al. (2020). To create this model, Pelgrims et al. (2020) fits a shell of higher dust density around the Sun using the 3D Cartesian map of dust differential extinction constructed by Lallement et al. (2019). The Lallement et al. (2019) dust map is based on data from Gaia DR2 (Gaia Collaboration et al. 2018) and 2MASS (Skrutskie et al. 2006) and spans $6 \times 6 \times 0.8$ kpc³ in the Heliocentric right-

handed Galactic-XYZ coordinates. It has a voxel volume of 125 pc³ and a spatial resolution of 25 pc. Example slices of this map with the Pelgrims et al. (2020) model overplotted are shown in Figure 2.

We also use the 3D model of the Local Bubble surface geometry constructed by O’Neill et al. (2024) for a brief investigation in Section 3. They use the 3D dust differential extinction provided by Edenhofer et al. (2023) to fit the distance to the Local Bubble in all directions as a region of higher dust density around the Sun.

In Section 4, we query the 12 posterior samples for the 3D dust maps provided by Edenhofer et al. (2023) via the publicly available `dustmaps` Python package (Green 2018) at their plane-of-sky native angular resolution of $14'$, which corresponds to a HEALPix pixelization scheme at $N_{\text{side}} = 256$. These 3D dust maps leverage distance and extinction estimates to stars from Zhang et al. (2023), which are derived from Gaia DR3 data (Gaia Collaboration et al. 2023). The distance resolution of these maps varies from 0.4 pc at 69 pc to 7 pc at 1.25 kpc. We query the map using uniform distance bins of 7 pc. The map is provided in unitless extinction values defined in Zhang et al. (2023). We multiply the map by a factor of 2.8 to convert it to Johnson’s V -band A'_V (Zhang et al. 2023). We then convert A'_V to volume density of hydrogen nuclei (n_{H}) using the extinction curve from Fitzpatrick et al. (2019) to convert $A_G = 0.796 A'_V$ and the relationship $A_G / N_{\text{H}} = 4 \times 10^{-22}$ cm² mag from Zucker et al. (2021) and Bialy et al. (2021). To match the resolution of the polarization fraction and smooth out small-scale fluctuations in the map, we smooth the HEALPix sphere at each distance bin to a FWHM = $80'$ then repixelate it to $N_{\text{side}} = 64$. Example slices of the map of the mean of the posterior samples are also shown in Figure 2 with the Pelgrims et al. (2020) model overplotted for comparison.

In Section 4, we also make comparisons with the 3D dust maps provided by Leike et al. (2020). These maps leverage distance and extinction estimates from the StarHorse catalog (Anders et al. 2019), which combines data from Gaia DR2 (Gaia Collaboration et al. 2018), ALLWISE (Cutri et al. 2013), PANSTARRS (Flewelling et al. 2020), and 2MASS (Skrutskie et al. 2006). The Leike et al. (2020) maps span $740 \times 740 \times 540$ pc³ in the Heliocentric Galactic-XYZ coordinates, respectively, with a voxel size of 1 pc³ and spatial resolution of 1 pc. We also query the 12 posterior samples of the Leike et al. (2020) maps via the `dustmaps` package. The Leike et al. (2020) maps are given in optical depth in the Gaia G band per 1 pc. We convert to n_{H} following Zucker et al. (2021) and Bialy et al. (2021).

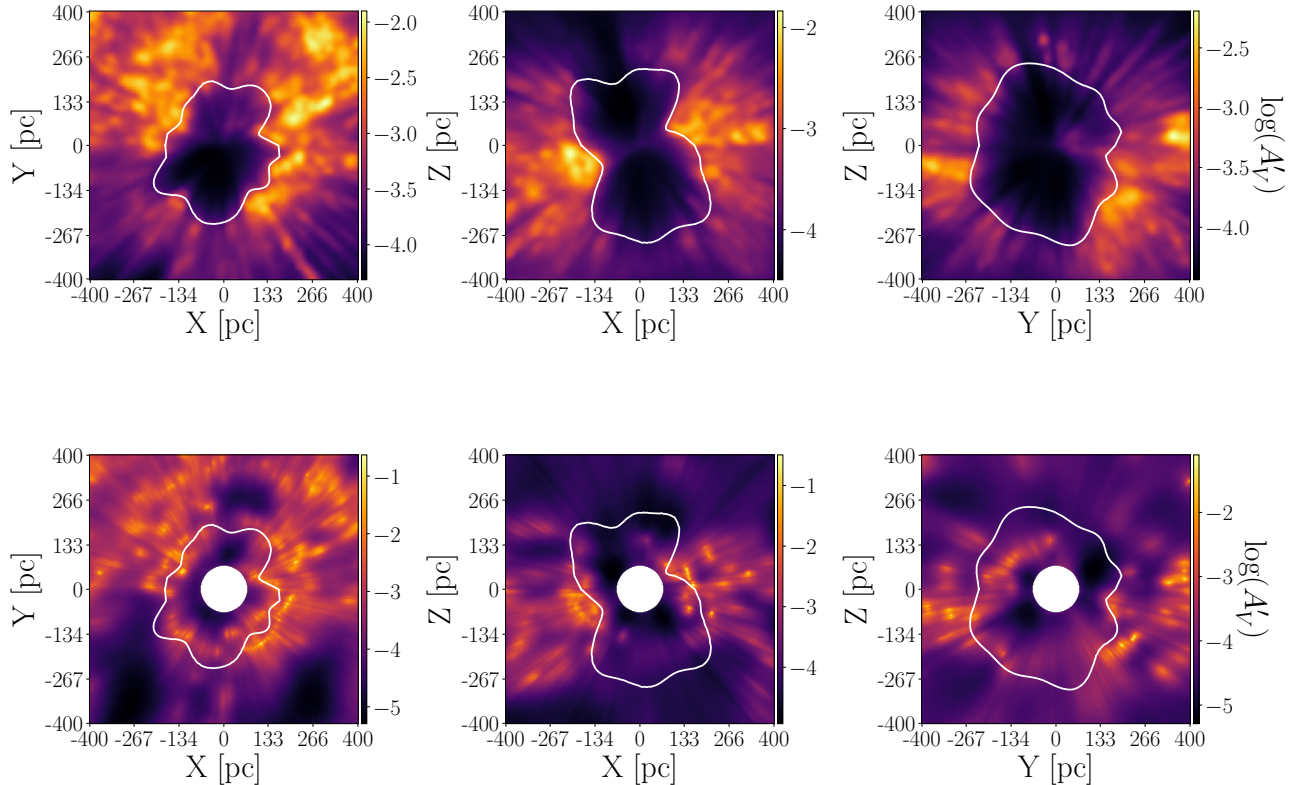


Figure 2. Slices through the XY (left), XZ (middle), and YZ (right) planes of the 3D reconstructed differential extinction maps of Lallement et al. (2019) (top) and Edenhofer et al. (2023) (bottom). The Sun is at the origin. The positive X axis points towards the Galactic center at $l = 0^\circ$, the positive Y axis points towards $l = 90^\circ$ in the Galactic plane, and the positive Z axis points out of the plane in the direction of the Galactic North pole. The slices show the log scale of the differential extinction, which is in units of magnitudes per parsec. The subpanels only extend up to 400 pc in each direction for a direct comparison. The model for the Local Bubble surface geometry of Pelgrims et al. (2020) is overplotted in white in each subpanel.

2.3. Rotation Measure

We use a map of the posterior mean of the Galactic Faraday sky developed by Hutschenreuter et al. (2023) for a brief investigation in Section 3. To produce these maps, they use information field theory, a Bayesian inference framework for fields (Enßlin 2019), on compiled catalogs of extragalactic Faraday rotation measures (Van Eck et al. 2023) and Galactic pulsar dispersion measures (Manchester et al. 2005), as well as data on Galactic bremsstrahlung emission (Planck Collaboration et al. 2016b) and the hydrogen α spectral line (Finkbeiner 2003).

3. NO IMPRINT OF THE LOCAL BUBBLE ON THE DUST POLARIZATION FRACTION

3.1. Motivation

We begin the exploration of the effect of different geometrical factors on the polarization fraction by searching for an imprint of the geometry of the dust wall surrounding the Local Bubble on the Planck 353 GHz dust polarization fraction. In this subsection, we discuss the assumptions made in previous studies regarding the Lo-

cal Bubble surface. These assumptions help us design a test for studying this effect in the next subsection. A significant detection of an imprint of the Local Bubble geometry on the polarization fraction would validate these assumptions.

The first assumption is that the observed polarized dust emission is dominated by dust in the Local Bubble wall at the relevant angular scales and Galactic latitudes. This assumption, made in several analyses (e.g., Alves et al. 2018; O’Neill et al. 2023), is supported by several studies using optical starlight polarization data (Leroy 1999; Andersson & Potter 2006; Santos et al. 2011; Frisch et al. 2015; Medan & Andersson 2019; Cotton et al. 2019). The alignment of neutral hydrogen structures at local velocities with starlight polarization toward stars at distances within a few hundred parsecs is consistent with a picture where most of these structures are positioned at comparable distances within the Local Bubble at high Galactic latitudes ($|b| > 30^\circ$) (Clark et al. 2014). Gontcharov & Mosenkov (2019) observed that starlight polarization fraction plateaus after 150-250 pc across the sky. By

comparing the 353 GHz polarized emission with the polarized optical starlight, Skalidis & Pelgrims (2019) find that most of the 353 GHz polarized emission signal is captured within the first 250 pc at $|b| > 60^\circ$, suggesting the presence of a dust wall around that distance.

The second assumption is that the magnetic field’s inclination is tangential to the surface of the Local Bubble. To fit a model of the Local Bubble magnetic field, Alves et al. (2018) assume that all the swept-up matter and field lines due to the supernova explosions that formed the Local Bubble are squeezed into a thin layer that follows its surface, leading the magnetic field lines to be tangent to the surface. O’Neill et al. (2023) also make this assumption to project the observed dust polarization angles onto the Bubble’s surface and build a 3D model of the Bubble wall magnetic field.

Other work has found magnetic field structure tangential to bubbles on supernova scales, observationally (e.g., Kothés & Brown 2009; Tahani et al. 2022a,b) and in simulations (Kim & Ostriker 2015). It has also been shown on the scales of HII regions, observationally (Tahani et al. 2023) and in simulations (Krumholz et al. 2007). On the scale of superbubbles, such as our Local Bubble, a comparison of the plane-of-the-sky and line-of-sight magnetic field strengths as well as measurements of the polarization fraction towards regions associated with the Orion-Eridanus superbubble suggest that the large-scale magnetic field in the region was primarily shaped by the expanding superbubble and is tangential to its surface (Heiles 1997; Soler et al. 2018). However, there is no direct evidence that the nearby magnetic field is preferentially tangential to the Local Bubble surface. The only constraints on the magnetic inclination angle using the geometry of the Local Bubble surface are at the Galactic polar caps from Alves et al. (2018) and Pelgrims et al. (2020). They each fit an analytical parametric model of the magnetic field, including terms related to the geometry of the Bubble wall, to dust polarization data from Planck. One of the parameters of the magnetic field model used by Pelgrims et al. (2020) is the magnetic inclination angle. They find that the magnetic field is oriented mostly in the plane of the sky at the Galactic polar caps. The polar caps are the regions in which the Local Bubble has perhaps the least-well-defined surface, as discussed further below.

The shape of the Local Bubble wall has been modeled differently in different works. Some studies fit a generalized parametric geometry, such as an ellipsoid (Alves et al. 2018), in an attempt to fit general properties of the Local Bubble magnetic field on large scales. Others model the detailed boundary of the Local Bubble using 3D maps of the dust extinction (Pelgrims et al. 2020;

O’Neill et al. 2024). These models therefore vary based on the variations of the different 3D dust reconstructions. Pelgrims et al. (2020) model the radial distance of the Local Bubble wall from the Sun in each direction as the first distance where the second derivative with respect to the distance of the differential extinction constructed by Lallement et al. (2019) reaches zero, i.e., the first inflection point, $d^2A'_V(r)/dr^2 = 0$. O’Neill et al. (2023) and Zucker et al. (2022) use the geometry defined by Pelgrims et al. (2020) in their work. O’Neill et al. (2024) employ a similar methodology to Pelgrims et al. (2020), using the differential extinction maps constructed by Edenhofer et al. (2023) instead to construct their model. Other studies use different tracers to model the geometry of the Bubble. Liu et al. (2017) assumes that the measured X-ray intensity is proportional to the distance to the Bubble in the considered direction. Several other tracers such as NaI absorption measurements (Sfeir et al. 1999; Lallement et al. 2003), stellar color excess measurements (Lallement et al. 2014), and diffuse interstellar bands (Farhang et al. 2019), have also been used for constructing models of the Bubble wall geometry. These geometries vary significantly from one another. While some model the Local Bubble as a closed surface (Pelgrims et al. 2020), others describe the same structure as a Local Chimney, i.e., open at high Galactic latitudes and funneling material into the Milky Way’s halo (e.g., Sfeir et al. 1999; Lallement et al. 2003; O’Neill et al. 2024). Also, the Local Bubble surface may have tunnels to surrounding cavities like the Gum Nebula and/or GSH238+00+09 rather than having a closed geometry (e.g., Welsh 1991; Lallement et al. 2003; O’Neill et al. 2024).

We aim to test whether the degree-scale structure of the Local Bubble is measurably imprinted in the statistics of polarized dust emission. We use the most recent models of the Local Bubble geometry constructed based on 3D dust mapping. For our main analysis, we use the Pelgrims et al. (2020) model, which has a closed geometry. However, we also perform a brief test using the O’Neill et al. (2024) model, whose geometry is not fully connected. In each case, we test whether a magnetic field that is tangential to the Local Bubble wall is a statistical driver of the observed variation in the dust polarization fraction.

3.2. Testing the Dependence of the Dust Polarization Fraction on the Magnetic Inclination Angle

Using 3D dust extinction maps and a model of the Local Bubble surface geometry, we can measure the angle between the line of sight and the Bubble’s surface in each direction. If the magnetic field lines were tangential

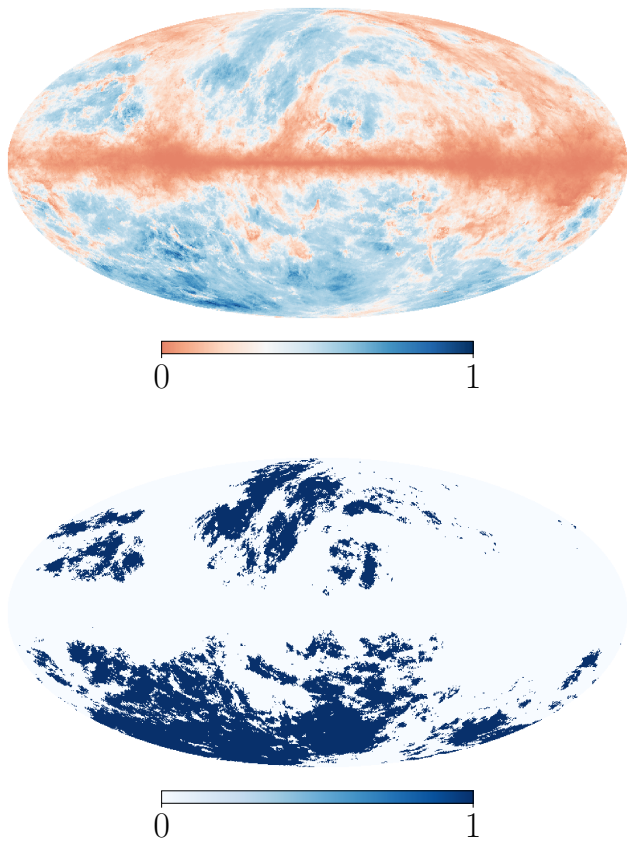


Figure 3. Maps used for selecting sightlines for the analysis described in Section 3. *Top panel:* A map of the ratio of the Lallement et al. (2019) 3D dust differential extinction map integrated within 50 pc of the Local Bubble surface defined by Pelgrims et al. (2020), A_V^{LB} , over the Planck dust extinction, A_V^{Planck} . This is plotted with a diverging colorbar centered on the 75th percentile (0.2), the cutoff we use in our sightline selection, with the allowed regions shown in blue. *Bottom panel:* A map of the mask of the selected region, combining $A_V^{\text{LB}}/A_V^{\text{Planck}} > 0.2$ (top panel) with $\text{SNR}_p > 3$ (Figure 1).

to the Local Bubble surface as discussed in Section 3.1, the angle between the line of sight and the Bubble’s surface should on average be correlated with the measured dust polarization fraction. Therefore, by quantifying the correlation between this angle and the dust polarization fraction for different sightlines, we can test whether there is measurable evidence that the magnetic field traced by the dust polarization is preferentially tangential to the Local Bubble surface.

The magnetic inclination angle γ , i.e., the angle between the magnetic field orientation and the plane of the sky, affects the measured dust polarization fraction.

The polarization fraction, p , is defined as

$$p = P/I = \sqrt{Q^2 + U^2}/I, \quad (1)$$

where P is the debiased polarized intensity as described in Section 2, Q and U are the Stokes parameters, and I is the total unpolarized intensity. Assuming uniform grain properties, the Stokes I , Q , and U parameters can be written as (Fiege & Pudritz 2000; Padoan et al. 2001; Pelkonen et al. 2007)

$$I = \int \epsilon \rho ds - \frac{1}{2} \int \alpha \epsilon \rho \left(\cos^2 \gamma - \frac{2}{3} \right) ds, \quad (2)$$

$$Q = \int \alpha \epsilon \rho \cos 2\psi \cos^2 \gamma ds, \quad (3)$$

$$U = \int \alpha \epsilon \rho \sin 2\psi \cos^2 \gamma ds, \quad (4)$$

where ρ is the volume density, ds is a distance segment along the line of sight, ϵ is the dust emissivity, α is a coefficient defined in Equation 15 of Padoan et al. (2001) that is a product of polarization efficiency factors, such as the degree of dust alignment and the dust grain polarization cross-section, and ψ is the angle between the projection of the magnetic field on the plane of the sky and North. These equations show the dependence of the polarization fraction on γ , ψ , α , and ϵ and their variations along the line of sight. At large angular scales, the variation in the observed dust polarization is dominated by γ and ψ (Hensley et al. 2019; Planck Collaboration et al. 2020a).

To maximize the chances of detecting this correlation, we limit our analysis to sightlines where the dust in the Local Bubble wall contributes the most to the total extinction and where we have high signal-to-noise ratio measurements of the dust polarization fraction ($\text{SNR}_p > 3$; Figure 1). We then select sightlines in the highest quartile of $A_V^{\text{LB}} / A_V^{\text{Planck}}$, i.e., sightlines where the extinction in the Local Bubble wall has the highest contribution to the total observed extinction (Section 2.1). For A_V^{LB} , we integrate the 3D dust differential extinction maps of Lallement et al. (2019) in the Local Bubble wall. We integrate over 50 pc in each direction, starting with the distance to the inner Local Bubble surface as defined by the 3D model of Pelgrims et al. (2020). Note that the threshold that corresponds to the highest quartile is $A_V^{\text{LB}} / A_V^{\text{Planck}} \sim 0.2$. This does not necessarily mean that $\gtrsim 20\%$ of the total extinction is attributable to the Local Bubble wall, as the integration over 50 pc may not represent the true Bubble thickness for all sightlines, and A_V^{Planck} is estimated through a scale factor multiplied by the GNILC dust optical depth map (Section 2.1). Nevertheless, this represents a best estimate

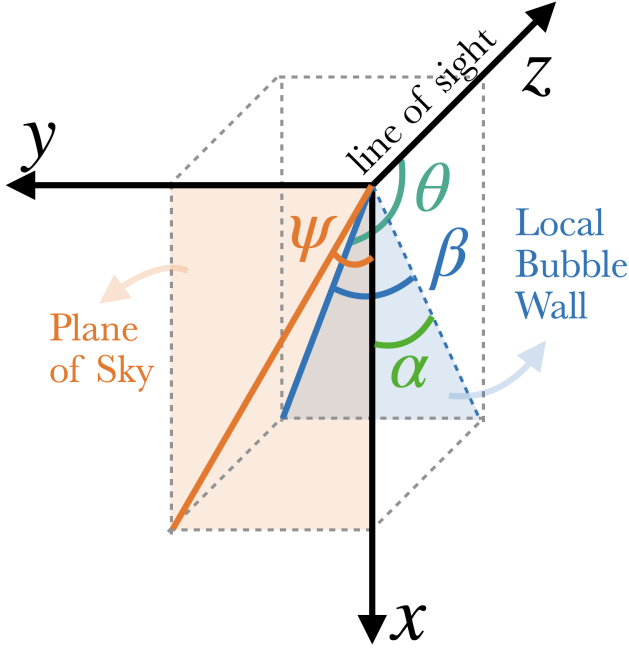


Figure 4. Diagram of the angles described and used in Section 3.3 for projecting the plane-of-sky magnetic field orientation (orange line) onto the Local Bubble wall (blue). The coordinates in this diagram follow the COSMO (HEALPix) convention, which is used in the Planck GNILC maps. These are not the Galactic coordinates used in Figure 2. For each position in the sky looking outwards, the local x-axis points South, the local y-axis points East, and the local z-axis points outwards.

of the sky regions for which the Local Bubble wall accounts for the largest fraction of the total extinction. This map and the final mask are shown in Figure 3.

3.3. Magnetic Fields in the Local Bubble Wall

We perform the following steps to estimate the angle between the line of sight and the Local Bubble wall.

1. For the Local Bubble geometry, we use the 3D model developed by Pelgrims et al. (2020). Since this model is constructed based on the 3D dust map of Lallement et al. (2019), we use this dust map in this subsection. Example slices of the map with the model overlaid are shown at the top of Figure 2. The resolution of this dust map is 25 pc. We use a 3D Gaussian filter to smooth the data to that resolution. This smooths out spurious small-scale fluctuations in the data product that may affect the results.
2. We calculate the gradient of the differential extinction data cube, $\nabla A'_{V,i}$ for each voxel i . This is a vector in the direction of the steepest change in the 3D volume at a given voxel. For the voxels at

the surface of the Local Bubble wall, $\nabla A'_{V,i}$ would therefore be orthogonal to that surface.

3. For each voxel i , we calculate the angle between the Local Bubble surface when projected onto the $x - z$ plane and the plane of the sky as

$$\alpha_i = \pi - \arccos \left(\frac{\nabla A'_{V,i} \cdot \vec{r}_i}{|\nabla A'_{V,i}| |\vec{r}_i|} \right), \quad (5)$$

where \vec{r}_i is the line of sight vector, using the Sun, which is at the center of the data cube, as the origin. This angle is shown in Figure 4 in green.

4. Pelgrims et al. (2020) models the distance to the Local Bubble surface for each direction on a HEALPix sphere. We sample our 3D Cartesian cube of α_i at the radial distance defined by the Pelgrims et al. (2020) model for each line-of-sight direction with a HEALPix pixelization scheme.

5. Using the Planck GNILC Stokes Q and U maps at 353 GHz, we calculate the plane-of-sky magnetic field orientation as

$$\psi = \frac{1}{2} \arctan \frac{-U}{-Q}. \quad (6)$$

This angle is shown in Figure 4 in orange.

6. We project the plane-of-sky magnetic field orientation onto the Local Bubble surface as

$$\beta = \arctan(\tan \psi \cos \alpha). \quad (7)$$

This angle is shown in Figure 4 in blue.

7. We calculate the angle between the line of sight and the magnetic field lines tangential to the surface of the Local Bubble as

$$\theta = \arccos(\cos \beta \sin \alpha). \quad (8)$$

This angle is shown in Figure 4 in teal.

3.4. No Detected Imprint of the Local Bubble Wall on the Polarization Fraction

We do not find any correlation between p_{353} and θ from Equation 8 over the mask defined in Figure 3. The Spearman rank coefficient, which is agnostic to the functional dependence between p_{353} and θ , is 3×10^{-3} . This indicates that at least one of the assumptions described in Section 3.1 is not valid. In other words, either the magnetic field is not generally tangent to the Local Bubble surface, the dust polarization is not dominated by the dust within 50 pc of the surface as defined by

the Pelgrims et al. (2020), or a combination of these possibilities.

We also test whether we find an anti-correlation between θ and the absolute value of the rotation measure but do not find any evidence for it. Therefore, we do not find an imprint of the detailed 3D geometry of the Local Bubble wall on the polarization statistics.

O’Neill et al. (2024) provide a map of the inclination angle between the Local Bubble wall as defined by their model and the plane of the sky. We also test for a correlation between this angle and the polarization fraction and do not find any.

4. IMPRINT OF DUST COMPLEXITY ON POLARIZATION FRACTION

We continue the investigation of how the 3D distribution of dust impacts the polarization fraction beyond the Local Bubble, taking into account the distribution of the dust in an extended volume around the Sun. We use the 3D dust maps constructed by Edenhofer et al. (2023) in this section. The benefits of these maps are that they have high resolution and extend radially up to 1.25 kpc away from the Sun.

If contributions to the polarized dust emission originate from regions along the line of sight with differently oriented magnetic fields, the integrated signal will be depolarized relative to emission from a region with uniform magnetic fields. We postulate that sightlines with multiple dust components that are separated in distance and contribute similarly to the total column density are more likely to have substantial dust emission originating from regions with differently oriented magnetic fields. We test the hypothesis that on average, for sightlines with the same column density, the ones for which the dust is distributed into multiple components at different distances with similar contributions to the total column density are associated with higher levels of depolarization than those for which the dust contribution to the total column density is concentrated.

4.1. Sightline Selection

We select sightlines with high-fidelity dust polarization measurements ($\text{SNR}_p > 3$), trustworthy 3D dust reconstruction, and a dominant contribution from the dust extinction within the 3D dust maps $A_V^{\text{Edenhofer}}$ to the total estimated extinction A_V^{Planck} (Section 2.1). The last constraint is to avoid sightlines at the lowest Galactic latitudes, where the dust extends in distance well beyond the regions where the dust is mapped in 3D out to 1.25 kpc. We mask sightlines where the ratio $A_V^{\text{Edenhofer}}/A_V^{\text{Planck}} < 0.5$.

Edenhofer et al. (2023) use estimates of stellar distances and extinctions from Zhang et al. (2023) to con-

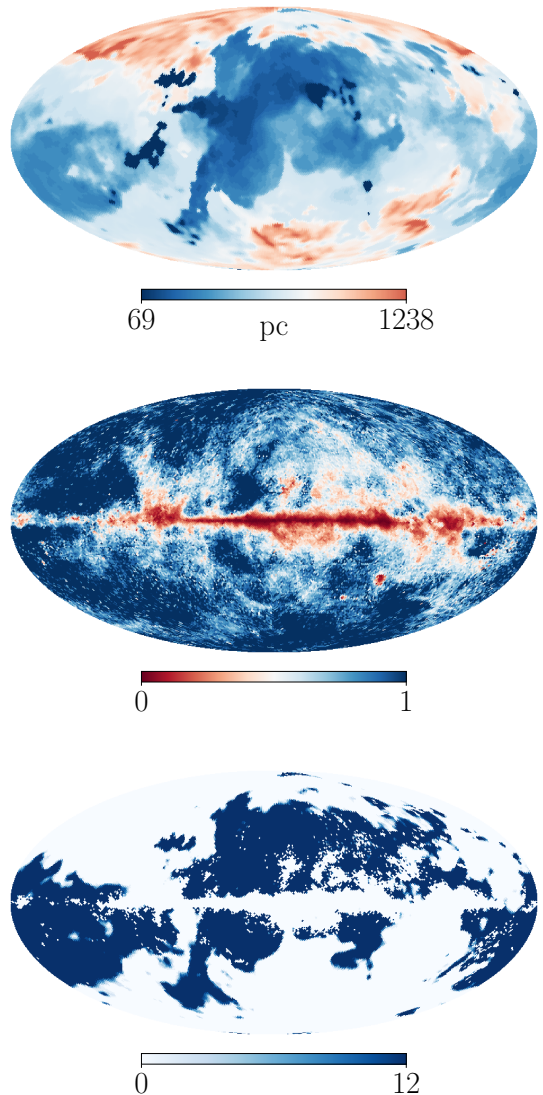


Figure 5. Maps used for selecting sightlines for the analysis described in Section 4. *Top panel:* A map of the distance at which the extinction in the first posterior sample of the Edenhofer et al. (2023) 3D dust maps reaches 50 mmag. This is plotted with a diverging colorbar centered on 200 pc, the cutoff we use in our sightline selection, with the allowed regions shown in blue. *Middle panel:* A map of the ratio of the Edenhofer et al. (2023) 3D dust differential extinction map integrated out to 1.25 kpc over the Planck dust extinction. This is plotted with a diverging colorbar centered on 0.5, the cutoff we use in our sightline selection, with the allowed regions shown in blue. *Bottom panel:* A sum of the masks of the selected regions over each of the 12 posterior samples, combining the selected regions from the quantities in the top panel, middle panel, and Figure 1.

struct their 3D dust maps. However, Edenhofer et al. (2023) found that their predictions disagree with Zhang

et al. (2023) where the radially integrated differential extinction is below 50 mmag or above 4 mag. We therefore use those thresholds to mask sightlines where the dust differential extinction is likely to be significantly over- or under-estimated. The distance to those thresholds for a given sightline varies slightly for the 12 different posterior samples, so we apply a slightly different mask to each posterior sample. We only consider sightlines where the differential extinction integrated radially outwards reaches 50 mmag within 200 pc of the Sun. A threshold higher than 200 pc would include more sightlines in the selection, but it would shorten the minimum path length considered. Because in Section 4.5, we compare our results with the Leike et al. (2020) maps, which only extend out to 270 pc, we find 200 pc to be a good balance between having a large enough sample size and minimum path length. The minimum path length considered through the Edenhofer et al. (2023) maps for estimating the dust complexity is therefore 1.05 kpc.

A map of the distance at which the extinction reaches 50 mmag for different sightlines is shown at the top of Figure 5. This is for the first posterior sample, but the equivalent maps for the remaining 11 posterior samples look visually indistinguishable. We center the diverging colorbar in this subplot to 200 pc to show which sightlines pass the threshold.

After masking sightlines with $\text{SNR}_p < 3$ or with $A_V^{\text{Edenhofer}}/A_V^{\text{Planck}} < 0.5$ for the 12 posterior samples, the integrated differential extinction within 1.25 kpc is higher than 4 mag for only about 10 sightlines per posterior sample. We exclude these sightlines from our analysis.

After performing all the cuts, we are left with about 19,100 sightlines per posterior sample for this analysis. Those sightlines are shown at the bottom of Figure 5. The map shown is the sum of the binary masks over the 12 posterior samples. Note that the only discrepancies between the 12 posterior samples are at the edges of the selected regions. The rest of the map is either 12 or 0.

4.2. Dust Complexity

We aim to quantify the complexity of the 3D dust distribution along each line of sight. For this, we take inspiration from Panopoulou & Lenz (2020), who perform a Gaussian decomposition of the neutral hydrogen (H I) emission spectra of each sightline to quantify its complexity. They use these components i , weighted by their column density N_{HI}^i , to define a metric

$$\mathcal{N}_c^{\text{HI}} = \sum_{i=1}^{n_{\text{clouds}}} \frac{N_{\text{HI}}^i}{N_{\text{HI}}^{\text{max}}}, \quad (9)$$

where $N_{\text{HI}}^{\text{max}}$ is the column density of the component with highest N_{HI} . This is a more relevant measurement of complexity than simply counting the number of components because it takes into account the relative contribution of each detected component, and the dust polarization signal arises from a density-weighted integral along the line of sight. If there are two components along the line of sight and they have equal column densities, then $\mathcal{N}_c^{\text{HI}} = 2$, whereas if one has half the column density of the other, then $\mathcal{N}_c^{\text{HI}} = 1.5$, and so forth. Therefore, $\mathcal{N}_c^{\text{HI}}$ could be, for instance, 2 for any number of components larger than 1. This metric was used to detect an imprint of line-of-sight magnetic field tangling in dust polarization in Pelgrims et al. (2021).

We use a metric inspired by Equation 9 to quantify the complexity of the 3D dust distribution, i.e., we decompose the 3D dust sightlines into “clouds,” or components along the line of sight, and then use a version of Equation 9, replacing N_{HI} with N_{H} inferred from the dust extinction (Section 2), i.e.,

$$\mathcal{N}_c = \sum_{i=1}^{n_{\text{clouds}}} \frac{N_{\text{H}}^i}{N_{\text{H}}^{\text{max}}}. \quad (10)$$

To decompose each of the 19,100 sightlines into different components, we use the dendrogram technique (Rosolowsky et al. 2008). We use the Python package `astrodendro`¹. Cahlon et al. (2023) applied the 3D version of this technique on the Leike et al. (2020) 3D dust maps to produce a uniform catalog of molecular clouds in the solar neighborhood. In this analysis, we apply the 1D version on individual sightlines.

Dendrogramming identifies density peaks in the data and connects them along hierarchical isosurfaces of constant n_{H} , forming a tree-like structure. We refer the reader to Rosolowsky et al. (2008) for a description of the core algorithm. We focus the explanation here on the algorithm’s three parameters. The first parameter defines the minimum absolute Hydrogen number density n_{H} threshold for a structure to be included as part of the tree. We set this parameter to 0. This is because the tree-like structure constructed by this algorithm is not useful for our purposes. We only consider the density peaks identified.

The remaining two parameters, Δ_n and $\#_{\text{voxels}}$, define the minimum prominence for a peak to be considered an independent component. Its largest n_{H} has to be Δ_n above the n_{H} of the adjacent isosurface for it to be considered an independent component from that isosurface. Similarly, $\#_{\text{voxels}}$ defines the threshold number of vox-

¹ <http://www.dendrograms.org/>

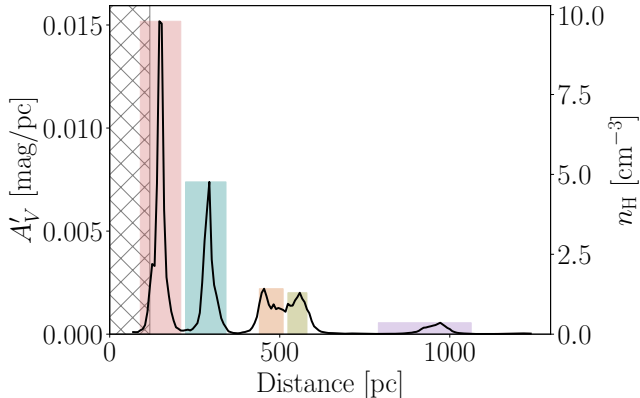


Figure 6. The dust distribution in units of differential extinction (mag/pc, left y-axis) and equivalent Hydrogen number density (cm^{-3} , right y-axis) along a representative sightline through the Edenhofer et al. (2023) maps. The Galactic coordinates of this sightline are $l = 163.12^\circ$ and $b = -11.42^\circ$. The region before the extinction reaches 50 mmag (hatched) is discarded from our analysis. The components identified by the dendrogram algorithm with $\Delta_n = 4.52 \times 10^{-3} \text{ cm}^{-3}$ ($A'_V = 7 \times 10^{-6}$), and $\#_{\text{voxels}} = 3$ (21 pc) are shaded in different colors.

els it has to span along a sightline to be considered an independent component, where each voxel spans 7 pc of the sightline. If a peak passes both of those thresholds, it is identified as a component by the algorithm.

For this analysis, we experiment with various values for Δ_n and $\#_{\text{voxels}}$ and plot the resulting peaks identified for each variation. We find a range between $\Delta_n = 1.94 \times 10^{-3} \text{ cm}^{-3}$ ($A'_V = 3 \times 10^{-6} \text{ mag/pc}$) and $\Delta_n = 3.87 \times 10^{-3} \text{ cm}^{-3}$ ($A'_V = 9 \times 10^{-6} \text{ mag/pc}$) and $\#_{\text{voxels}} = 3$ (21 pc) and a range between $\#_{\text{voxels}} = 5$ (35 pc) recover the visually identified peaks. We report our results for the fiducial values of $\Delta_n = 4.52 \times 10^{-3} \text{ cm}^{-3}$ ($A'_V = 7 \times 10^{-6}$), and $\#_{\text{voxels}} = 3$ (21 pc). However, we find our results to be robust to all the variations we test for within the ranges mentioned.

We run the dendrogram algorithm on each sightline separately, considering the entire sightline from 69 pc to 1.25 kpc. However, we only keep identified components with peaks that are radially farther than the distance at which the extinction in that sightline reaches 50 mmag (Section 4.1). If the distance of the peak of a component is farther than this threshold but part of the component is below that threshold (Figure 6), we still consider the part of the component that is below that threshold when integrating over the n_{H} of that component.

We calculate Equation 10 for each sightline to quantify its dust complexity. For the sightline in Figure 6,

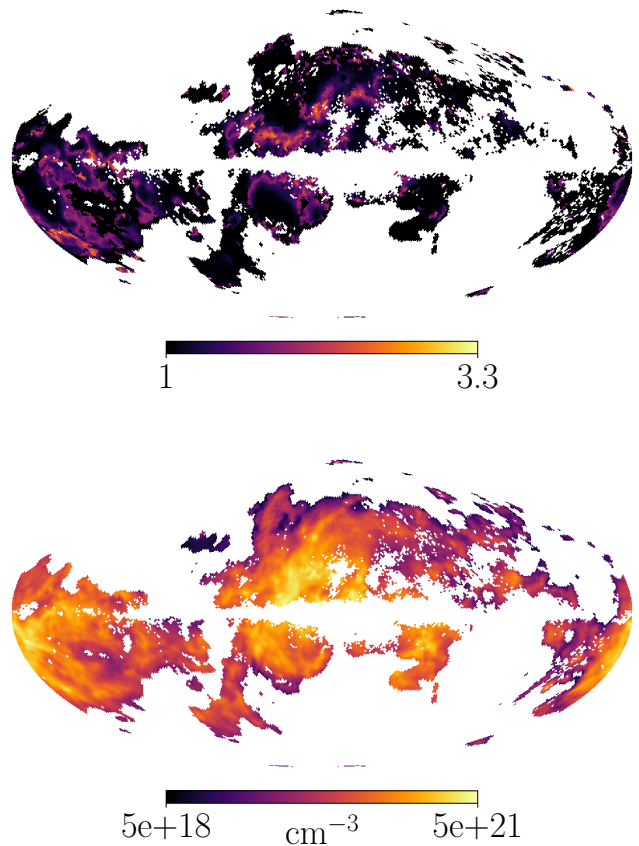


Figure 7. *Top panel:* A map of \mathcal{N}_c calculated using the dendrogram algorithm with $\Delta_n = 4.52 \times 10^{-3} \text{ cm}^{-3}$ ($A'_V = 7 \times 10^{-6}$), and $\#_{\text{voxels}} = 3$ (21 pc). *Bottom panel:* A log-scale map of $N_{\text{H}}^{\text{Edenhofer}}$ formed by integrating over the entire dataset (up to 1.25 kpc) with units of cm^{-2} . These maps are shown only for the sightlines selected in Section 4.1 and for one of the posterior samples of Edenhofer et al. (2023).

for example, $\mathcal{N}_c=2.16$. We show a map of \mathcal{N}_c for the sightlines we select in Section 4.1 at the top of Figure 7.

4.3. Nearest-Neighbor Matching

To examine the effect of line-of-sight dust complexity on polarization fraction, we compare sightlines that have the same total column densities but very different 3D dust distributions. We define low- and high-dust complexity sightlines as sightlines with $\mathcal{N}_c \leq 1.1$ and $\mathcal{N}_c \geq 1.5$, respectively. The goal is to compare sightlines with different dust distributions, so the particular \mathcal{N}_c threshold values are less important. We start with these values for our fiducial analysis because they are similar to the thresholds used in Pelgrims et al. (2021). The Pelgrims et al. (2021) analysis used a Gaussian decomposition of 3D maps of the neutral hydrogen

emission line, where the third dimension is radial velocity. They used $\mathcal{N}_c=1$ and $\mathcal{N}_c \geq 1.5$ in their analysis. However, for the data and mask we use in our analysis, we find that across the 12 posterior sample maps from [Edenhofer et al. \(2023\)](#), only 8-31 sightlines have $\mathcal{N}_c=1$, i.e., a single dust component. Since this does not represent a large enough sample size, we define the low-complexity bin as sightlines with $\mathcal{N}_c \leq 1.1$. This increases the number of sightlines in that bin to around 1,000 per posterior sample. However, we also confirm that our results are robust to variations in these thresholds (Section 4.6).

Because the \mathcal{N}_c bins are widely separated, small fluctuations in \mathcal{N}_c due to the choices of Δ_n and $\#\text{voxels}$ do not cause sightlines from one bin to shift to the other bin. However, we also verify that our results are robust to different choices of Δ_n and $\#\text{voxels}$.

We treat the column density as a confounding variable when comparing the distribution of p_{353} for the low- and high-complexity bins. Any difference in the p_{353} distributions for the low- and high-complexity bins could potentially be explained by a difference in the column density integrated over the distance used to calculate \mathcal{N}_c or a difference in the total column density over a sightline. Therefore, both need to be taken into account for a fair comparison of p_{353} between the two complexity bins.

We integrate n_{H} for each sightline up to 1.25 kpc, starting from either the distance at which the extinction reaches 50 mmag or the minimum distance of the first detected component whose peak lies farther than that distance as explained in Section 4.2, whichever is closer. We call this $N_{\text{H}}^{\text{Edenhofer}}$ and show a map of it for the sightlines considered in our analysis in the bottom panel of Figure 7.

Since $N_{\text{H}}^{\text{Edenhofer}}$ only takes into account dust up to 1.25 kpc, we also consider the total column density over a sightline. We convert A_V^{Planck} (Section 2.1) to $N_{\text{H}}^{\text{Planck}}$ following the formalism in Section 2.2. In Section 4.6, we also experiment with adding the absolute value of the Galactic latitude as an additional confounding variable.

We perform nearest-neighbor matching with no replacement between the sightlines in the low- and high-complexity bins. We pair up each low-complexity sightline to the high-complexity sightline with the closest $N_{\text{H}}^{\text{Edenhofer}}$ and $N_{\text{H}}^{\text{Planck}}$ values based on the Manhattan distance using the ball-tree algorithm. For each matched pair, we subtract the p_{353} of the sightline with the lower complexity from the p_{353} of the sightline with the higher complexity. We take the average of the differences over the matched pairs, Δp_{353} , to test whether

sightlines with higher dust complexity have higher depolarization levels on average than sightlines with lower dust complexity, i.e., $\Delta p_{353} < 0$.

4.4. Statistical Tests

We determine the statistical significance of our results through permutation tests. We perform the analysis described in Section 4.3 and obtain Δp_{353}^s for each of the 12 posterior samples s . We also perform null tests and obtain a distribution of $\Delta p_{353}^{s,\text{null}}$ for each posterior sample s . We calculate a p-value as the proportion of $\Delta p_{353}^{s,\text{null}}$ that are equal to or more extreme than Δp_{353}^s .

For the null tests, instead of separating sightlines into high- and low-complexity bins, we randomly select 25% of sightlines (5,050 sightlines) to be in bin 1 and 25% to be in bin 2. We then run the same analysis on those 2 groups, pairing them up based on $N_{\text{H}}^{\text{Edenhofer}}$ and $N_{\text{H}}^{\text{Planck}}$ and subtracting p_{353} of the sightline in bin 1 from p_{353} of the sightline in bin 2 for each pair. To ensure we are not biasing the null test by matching neighboring sightlines which have similar p_{353} , for each run, we randomly alternate between selecting the sightlines in bin 1 to be in the Northern Galactic hemisphere and the sightlines in bin 2 to be in the Southern Galactic hemisphere and the other way around.

We consider results with a two-tailed p-value < 0.001 to be statistically significant. We repeat this analysis for several reasonable values for Δ_n and $\#\text{voxels}$ and for different thresholds of the \mathcal{N}_c bins to ensure that our results are independent of those choices.

In addition to checking the statistical significance of Δp_{353}^s for each of the 12 posterior samples, we also report the mean and standard deviation of Δp_{353}^s across the posterior samples. The error propagated due to the uncertainty on p_{353} is 2 orders of magnitude less than the result. The uncertainty is dominated by the variation in the result across the 12 samples.

4.5. Results

We perform the analysis described in the previous subsections on the [Edenhofer et al. \(2023\)](#) maps which extend radially to 1.25 kpc and compare the polarization fractions of sightlines with $\mathcal{N}_c \leq 1.1$ and those with $\mathcal{N}_c \geq 1.5$. An example of a pair of matched sightlines with the same $N_{\text{H}}^{\text{Edenhofer}}$ and $N_{\text{H}}^{\text{Planck}}$ is shown in Figure 8. Even though the polarization fraction of the higher-complexity sightline is lower than that of the lower-complexity sightline in this example, not all sightlines follow this trend. We are only looking for a statistically significant average effect.

For this test, Δp_{353}^s , the mean over the paired sightlines for each posterior sample s , is plotted in orange

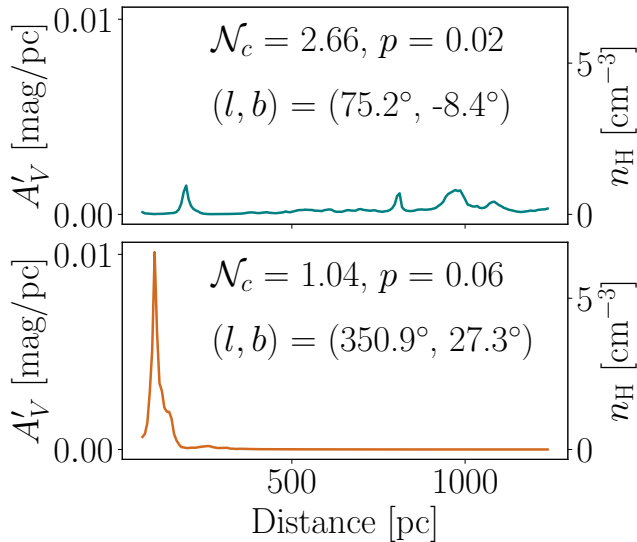


Figure 8. The dust distribution in units of differential extinction (mag/pc, left y-axis) and equivalent Hydrogen number density (cm^{-3} , right y-axis) along a pair of matched sightlines through the first posterior sample of the [Edenhofer et al. \(2023\)](#) map. These sightlines have the same $N_{\text{H}}^{\text{Edenhofer}}$, but the top one has a higher complexity than the bottom one. The Galactic coordinates, dust complexity, and polarization fraction of each of the sightlines are denoted on their subpanels.

at the top of Figure 9. The mean and standard deviation of Δp_{353}^s over the 12 samples are -1.47×10^{-2} and 0.22×10^{-2} , respectively. All 12 posterior samples pass the permutation test described in Section 4.4 with a p-value < 0.001 . A random $\Delta p_{353}^{s, \text{null}}$ for each posterior sample is shown in blue at the top of Figure 9 as well. Therefore, we find that higher dust complexity at equivalent column densities is associated with depolarization at the 1.5% level. This is at the level of 6.8% of the maximum polarization fraction measured by [Planck Collaboration et al. \(2020a\)](#) at 353 GHz and $80'$.

To determine whether this result is uniquely enabled by the [Edenhofer et al. \(2023\)](#) dust maps since they extend radially to 1.25 kpc, we repeat the analysis using the 3D [Leike et al. \(2020\)](#) dust maps, which extend to 370 pc in the positive and negative Galactic-X and Y coordinates and 270 pc in the positive and negative Galactic-Z coordinate. For consistency between different sightlines in those maps, we truncate all sightlines at 270 pc. Also, we start each sightline at 70 pc since [Leike et al. \(2020\)](#) find that the reconstructed dust density closer than 70 pc resembles a smeared-out version of the farther dust, an artifact related to systematic data biases. [Leike et al. \(2020\)](#) also provide 12 posterior samples for their maps which we use for this analysis.

The results for repeating the analysis using the [Leike et al. \(2020\)](#) maps instead are shown at the bottom of Figure 9. The mean and standard deviation of Δp_{353}^s over the 12 posterior samples are 2.75×10^{-3} and 3.06×10^{-3} , respectively. None of the 12 samples pass the permutation test, i.e., they are indistinguishable from the distributions of $\Delta p_{353}^{s, \text{null}}$. We also show a random $\Delta p_{353}^{s, \text{null}}$ for each posterior sample in blue in the same subplot of Figure 9.

To determine whether the null result is attributed to using a different dataset or to the lower extent in radial distance, we run the analysis on the [Edenhofer et al. \(2023\)](#) maps up to 270 pc, the same distance used for the [Leike et al. \(2020\)](#) maps. We plot the results in the middle of Figure 9. The mean and standard deviation of Δp_{353}^s over the 12 posterior samples are 1.05×10^{-3} and 1.36×10^{-3} , respectively. Again, none of the 12 samples pass the permutation test, i.e., they are indistinguishable from the distributions of $\Delta p_{353}^{s, \text{null}}$. The consistency of this result with null as well indicates that the null result we found using the [Leike et al. \(2020\)](#) maps is due to only considering distances up to 270 pc, not the choice of 3D dust dataset. This illustrates the role that dust components farther than 270 pc play in affecting polarization measurements.

4.6. Validation

In this subsection, we summarize some of the tests we performed to verify our results. As described in Section 4.2, we find that our results are robust to reasonable variations in Δ_n and $\#\text{voxels}$. The results are also consistent when using the Planck R3.01 353 GHz maps instead of the GNILC maps.

To ensure that the pairs were matched correctly, we examine the distributions of the differences in $N_{\text{H}}^{\text{Edenhofer}}$ and $N_{\text{H}}^{\text{Planck}}$ between the matched pairs. We verify that those differences peak near zero and are not skewed toward the positive or negative directions. We find that to be the case for both variables and over all 12 posterior samples of [Edenhofer et al. \(2023\)](#). We also find our results to be robust when including $|b|$ as a confounding variable in addition to $N_{\text{H}}^{\text{Edenhofer}}$ and $N_{\text{H}}^{\text{Planck}}$ in the pair matching – in other words, the result is not attributable to a dependence of the polarization fraction on Galactic latitude.

We also examine the angular separations between the sightline pairs and the discrepancies in their overall path lengths. The distributions of angular distances are consistent with a random distribution of angular distances for all 12 posterior samples of [Edenhofer et al. \(2023\)](#). We also find no significant differences in the total path

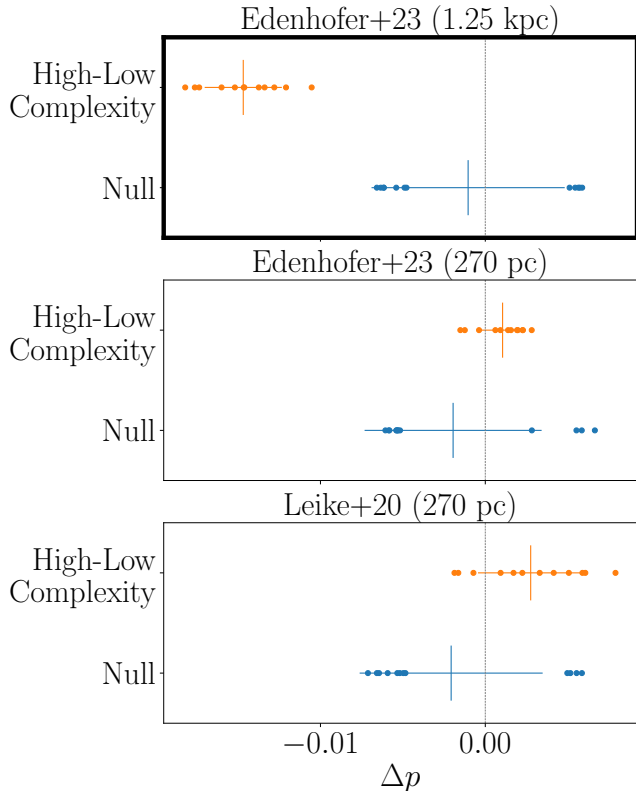


Figure 9. The mean difference in p_{353} over the paired sightlines for each of the 12 posterior samples, where for each pair, p_{353} for the lower-complexity sightline is subtracted from p_{353} for the higher-complexity sightline. \mathcal{N}_c is calculated on the Edenhofer et al. (2023) maps up to 1.25 kpc (top), the Edenhofer et al. (2023) maps up to 270 pc (middle), and the Leike et al. (2020) maps up to 270 pc (bottom). For each panel, the mean differences for the actual test are plotted in orange, and those for the null test are plotted in blue. The mean and standard deviation of the 12 means for each test are also plotted. The top panel agrees with our hypothesis: that sightlines with similar column densities will, on average, exhibit lower dust polarization fractions when their 3D dust distribution is more complex.

lengths between the paired sightlines across all 12 samples.

We experiment with varying the \mathcal{N}_c thresholds that define the bin edges of the low- and high-complexity sightlines. The 25th and 75th percentiles of the \mathcal{N}_c distribution over our mask vary slightly over the 12 posterior samples of Edenhofer et al. (2023) and over variations in Δ_n and $\#\text{voxels}$. However, they are roughly 1.4 and 2.3, respectively. Therefore, we split our sightlines based on these values into low- ($\mathcal{N}_c \leq 1.4$) and high-complexity ($\mathcal{N}_c \geq 2.3$) bins to achieve a roughly equal number of sightlines in each group. This should improve the pair-matching outcomes since there are more sight-

lines to match from in the smaller group. We find that our results are robust to this change.

Since neighboring sightlines are likely to have similar \mathcal{N}_c and similar p values, we test whether large regions of neighboring sightlines belonging to either the low- or high-complexity groups bias our results. We randomly sample 1,000 sightlines out of about 9,000 sightlines from each of the the low- and high-complexity groups before pair matching. We find that our results are robust to this test.

Finally, we modify the definition of \mathcal{N}_c from Equation 10 to

$$\mathcal{N}_c = \frac{N_{\text{H}}^{\text{Edenhofer}}}{N_{\text{H}}^{\text{max}}}, \quad (11)$$

i.e., we use the total column density out to 1.25 kpc rather than a sum over the dust components in the numerator. With the new definition, \mathcal{N}_c is only sensitive to the dendrogram-identified component with the highest column density $N_{\text{H}}^{\text{max}}$ rather than also being sensitive to the other dendrogram-identified components. Since the dendrogram parameters define the minimum prominence for a peak to be considered an independent component, we expect $N_{\text{H}}^{\text{max}}$ to be the least sensitive component to those parameters. Therefore, the new definition is much less sensitive to the dendrogram parameters. We test whether our results are robust to using the new definition and confirm that they are.

5. DISCUSSION AND CONCLUSIONS

In this paper, we explore how different geometrical factors affect the polarization fraction. In Section 3, we test whether we detect an imprint of the Local Bubble geometry on the polarization fraction. Following the well-motivated assumptions that the magnetic field lines are tangential to the Local Bubble surface and that this surface is defined by the model of Pelgrims et al. (2020), we test for a correlation between the measured polarization fraction and the angle the line of sight makes with the tangential magnetic field lines. However, we do not find evidence for this in sightlines where the dust extinction is dominated by the Local Bubble. We also do not find a correlation between the polarization fraction and the inclination angle between the Local Bubble wall defined by the model of O’Neill et al. (2024) and the plane of the sky. Therefore, we conclude that at least one of the commonly made assumptions must not hold. We hypothesize that dust structure beyond the Local Bubble wall plays a substantial role in determining the polarization structure of the dust emission. Our results show that simply projecting the Planck polarization data onto the Local Bubble geometry is not a

well-motivated model for the magnetic field structure of the Local Bubble.

In Section 4, we test how dust complexity, i.e., how the 3D dust is distributed along the line of sight, affects the polarization fraction. We quantify the dust complexity for each sightline and group the sightlines into low- and high-complexity groups. We pair-match the sightlines across the two groups based on their column densities. For each pair, we subtract the polarization fraction of the sightline with low complexity from that of the sightline with high complexity. We find that on average, the polarization fraction of the sightlines with higher complexity is 2% lower than those with lower complexity. This is only true when considering dust out to 1.25 kpc. The result is not statistically different from null when considering dust out to 270 pc only. Note that our definition of complexity does not take into account the distance to different dust components. Future work could incorporate the effect of this distance into the analysis.

We test whether the order of magnitude of this result agrees with our expectation based on geometric depolarization. Padoan et al. (2001) model the polarized thermal dust emission from protostellar cores formed through supersonic turbulent flows within molecular clouds following the formalism in Fiege & Pudritz (2000). Fiege & Pudritz (2000) develops this formalism to model the submillimeter polarization patterns for filamentary molecular clouds. Fiege & Pudritz (2000) and Padoan et al. (2001) ignore the effects of self-absorption and scattering since this model is for submillimeter wavelengths. Padoan et al. (2001) further assume that the dust grain properties are constant and the temperature is uniform. Since these assumptions are valid for our order of magnitude estimation, we follow the same formalism here.

Combining Equations 12, 13, and 14 of Padoan et al. (2001), the polarization fraction for a given sightline can be written as

$$p = \alpha \frac{\sqrt{q^2 + u^2}}{\int \rho ds - \alpha \frac{1}{2} \int \rho (\cos^2 \gamma - \frac{2}{3}) ds}, \quad (12)$$

where $q = Q/I$, $u = U/I$, ρ is the volume density, ds is a distance segment along the line of sight, α is a coefficient defined in Equation 15 of Padoan et al. (2001) that is a product of polarization reduction factors, such as the degree of dust alignment, and the dust grain polarization cross-section, and γ is the angle between the magnetic field vector and the plane of the sky.

From Equations 8 and 9 of Padoan et al. (2001), we have

$$q = \int \rho \cos 2\psi \cos^2 \gamma ds, \quad (13)$$

$$u = \int \rho \sin 2\psi \cos^2 \gamma ds, \quad (14)$$

where ψ is the angle between the projection of the magnetic field on the plane of the sky and North.

For this test, we consider sightlines with 2 clouds but different \mathcal{N}_c values. For simplicity, we assume each cloud to have a constant volume density, plane-of-sky magnetic field angle, and magnetic inclination angle along a certain sightline. Therefore, for a given sightline, we write

$$q = N_{H,a} \cos 2\psi_1 \cos^2 \gamma_a + N_{H,b} \cos 2\psi_2 \cos^2 \gamma_b, \quad (15)$$

$$u = N_{H,a} \sin 2\psi_1 \cos^2 \gamma_a + N_{H,b} \sin 2\psi_2 \cos^2 \gamma_b, \quad (16)$$

where $N_{H,a}$ and $N_{H,b}$ are the column densities for each cloud, and γ_a and γ_b are the magnetic inclination angles of the two clouds. Similarly, Equation 12 can be written as

$$p = \frac{0.15 \sqrt{q^2 + u^2}}{N_H - \frac{0.15}{2} (N_{H,a} \cos^2 \gamma_a + N_{H,b} \cos^2 \gamma_b - \frac{2}{3} N_H)}, \quad (17)$$

where we set $\alpha = 0.15$ as in Padoan et al. (2001), which corresponds to a $p_{\max} = 0.15$.

We take $N_{H,a} > N_{H,b}$, i.e.,

$$\mathcal{N}_c = \frac{N_{H,a} + N_{H,b}}{N_{H,a}}, \quad (18)$$

and divide the numerator and denominator of Equation 17 by $N_{H,a}$ to be able to write it in terms of \mathcal{N}_c , where $N_H/N_{H,a} = \mathcal{N}_c$ and $N_{H,b}/N_{H,a} = 1 - \mathcal{N}_c$.

We randomly sample an orientation for ψ_1 , ψ_2 , γ_a , and γ_b and a value between 1 and 1.1 for \mathcal{N}_c to calculate an instance of $p(\mathcal{N}_c \leq 1.1)$. We also sample different orientations and a value between 1.5 and 2 for \mathcal{N}_c to calculate an instance of $p(\mathcal{N}_c \geq 1.5)$. We then subtract $p(\mathcal{N}_c \leq 1.1)$ from $p(\mathcal{N}_c \geq 1.5)$ as in Section 4. We repeat this 10,000 times and average the results. We get

$$\langle p(\mathcal{N}_c \geq 1.5) - p(\mathcal{N}_c \leq 1.1) \rangle = -0.015. \quad (19)$$

This agrees with the result we measure in Section 4. Thus our empirical result is consistent with our theoretical estimate for the dust depolarization attributable to the line-of-sight dust complexity.

The line-of-sight magnetic field component is not directly measurable from the dust polarization. Variations in the orientation of magnetic fields along the line of sight induce differences in the polarization angles of different dust components along the same sightline (Lee & Draine 1985; Tassis & Pavlidou 2015; King et al. 2018). When the emission of those components has different spectral energy distributions (SEDs), a

frequency-dependent variation of the observed dust polarization angle along that sightline emerges, a phenomenon known as line-of-sight frequency decorrelation. This decorrelation complicates the translation of polarized dust emission maps from one frequency to another. Current analysis within the BICEP/Keck field does not demonstrate evidence of this phenomenon (BICEP/Keck Collaboration et al. 2021, 2023). However, a statistically significant detection of line-of-sight frequency decorrelation has been identified in larger sky areas across sightlines intersecting multiple dust clouds with varying magnetic field orientations (Pelgrims et al. 2021). Since polarized dust emission is the major foreground for CMB polarization measurements at high frequencies, it is important to characterize how the spatial complexity of the magnetic field in the dust might affect the frequency dependence of the foreground signal. In this paper, we have presented evidence that the spatial complexity of the dust affects the dust polarization signal.

The analysis in this paper highlights the importance of 3D dust mapping out to large distances. The dust distribution affects the dust polarization fraction, which has implications for the 3D magnetic field distribution. Since we expect higher complexity sightlines to have a lower polarization fraction on average, we would know that the magnetic field is more uniform along a sightline if it has both a highly complex dust distribution and a large polarization fraction. This analysis was performed on the sightlines shown in Figure 5. Improvements to 3D dust modeling will allow us to look for this effect at the very high Galactic latitudes excluded here.

Given the significance of the 3D dust distribution on measurements of the polarized dust emission, these data can be combined with position-position-velocity maps of the neutral hydrogen-based dust polarization templates. These templates, constructed based on the orientation of neutral hydrogen filaments, have been shown to correlate very well with the measured

dust polarization (Clark & Hensley 2019; Cukierman et al. 2023; BICEP/Keck Collaboration et al. 2023; Halal et al. 2024). Since the neutral hydrogen and dust trace similar volumes of the diffuse interstellar medium (Boulanger et al. 1996; Lenz et al. 2017), future work could morphologically match the position-position-position dust maps with the position-position-velocity neutral hydrogen-based maps to form 4D position-position-position-velocity maps of the magnetic field and polarized dust emission. Starlight polarization can also be used to provide a tomographic view of the plane-of-the-sky magnetic field and polarized dust emission for sightlines with these measurements (Panopoulou et al. 2019; Tassis et al. 2018). These data combined with Faraday tomography (Van Eck et al. 2017) or rotation measures (Tahani et al. 2018) can be used to constrain the 3D magnetic field structure.

We thank Gordian Edenhofer and Minjie Lei for insightful discussions. This work was supported by the National Science Foundation under grant No. 2106607. MT is supported by the Banting Fellowship (Natural Sciences and Engineering Research Council Canada) hosted at Stanford University and the Kavli Institute for Particle Astrophysics and Cosmology (KIPAC) Fellowship. This publication utilizes data from Planck, an ESA science mission funded by ESA Member States, NASA, and Canada. The computations in this paper were run on the Sherlock cluster, supported by the Stanford Research Computing Center at Stanford University.

Software: astropy (Astropy Collaboration et al. 2013, 2018), HEALPix² (Górski et al. 2005), healpy (Zonca et al. 2019), matplotlib (Hunter 2007), numpy (Oliphant 2015), scipy (Virtanen et al. 2020), dustmaps (Green 2018), astrodendro (Rosolowsky et al. 2008)

REFERENCES

- Alves, M. I. R., Boulanger, F., Ferrière, K., & Montier, L. 2018, *A&A*, 611, L5, doi: [10.1051/0004-6361/201832637](https://doi.org/10.1051/0004-6361/201832637)
- Anders, F., Khalatyan, A., Chiappini, C., et al. 2019, *A&A*, 628, A94, doi: [10.1051/0004-6361/201935765](https://doi.org/10.1051/0004-6361/201935765)
- Andersson, B. G., Lazarian, A., & Vaillancourt, J. E. 2015, *ARA&A*, 53, 501, doi: [10.1146/annurev-astro-082214-122414](https://doi.org/10.1146/annurev-astro-082214-122414)
- Andersson, B. G., & Potter, S. B. 2006, *ApJL*, 640, L51, doi: [10.1086/503199](https://doi.org/10.1086/503199)
- Astropy Collaboration, Robitaille, T. P., Tollerud, E. J., et al. 2013, *A&A*, 558, A33, doi: [10.1051/0004-6361/201322068](https://doi.org/10.1051/0004-6361/201322068)
- Astropy Collaboration, Price-Whelan, A. M., Sipőcz, B. M., et al. 2018, *AJ*, 156, 123, doi: [10.3847/1538-3881/aabc4f](https://doi.org/10.3847/1538-3881/aabc4f)
- Barnes, A. T., Watkins, E. J., Meidt, S. E., et al. 2023, *ApJL*, 944, L22, doi: [10.3847/2041-8213/aca7b9](https://doi.org/10.3847/2041-8213/aca7b9)

² <http://healpix.sourceforge.net/>

- Berdyugin, A., Piirola, V., & Teerikorpi, P. 2014, *A&A*, 561, A24, doi: [10.1051/0004-6361/201322604](https://doi.org/10.1051/0004-6361/201322604)
- Bialy, S., Zucker, C., Goodman, A., et al. 2021, *ApJL*, 919, L5, doi: [10.3847/2041-8213/ac1f95](https://doi.org/10.3847/2041-8213/ac1f95)
- BICEP/Keck Collaboration, Ade, P. A. R., Ahmed, Z., et al. 2021, *PhRvL*, 127, 151301, doi: [10.1103/PhysRevLett.127.151301](https://doi.org/10.1103/PhysRevLett.127.151301)
- . 2023, *ApJ*, 945, 72, doi: [10.3847/1538-4357/acb64c](https://doi.org/10.3847/1538-4357/acb64c)
- Boullanger, F., Abergel, A., Bernard, J. P., et al. 1996, *A&A*, 312, 256
- Breitschwerdt, D., Feige, J., Schulreich, M. M., et al. 2016, *Nature*, 532, 73, doi: [10.1038/nature17424](https://doi.org/10.1038/nature17424)
- Cahlon, S., Zucker, C., Goodman, A., Lada, C., & Alves, J. 2023, arXiv e-prints, arXiv:2308.14794, doi: [10.48550/arXiv.2308.14794](https://doi.org/10.48550/arXiv.2308.14794)
- Chen, C.-Y., King, P. K., Li, Z.-Y., Fissel, L. M., & Mazzei, R. R. 2019, *MNRAS*, 485, 3499, doi: [10.1093/mnras/stz618](https://doi.org/10.1093/mnras/stz618)
- Clark, S. E. 2018, *ApJL*, 857, L10, doi: [10.3847/2041-8213/aabb54](https://doi.org/10.3847/2041-8213/aabb54)
- Clark, S. E., & Hensley, B. S. 2019, *ApJ*, 887, 136, doi: [10.3847/1538-4357/ab5803](https://doi.org/10.3847/1538-4357/ab5803)
- Clark, S. E., Peek, J. E. G., & Putman, M. E. 2014, *ApJ*, 789, 82, doi: [10.1088/0004-637X/789/1/82](https://doi.org/10.1088/0004-637X/789/1/82)
- Cotton, D. V., Marshall, J. P., Frisch, P. C., et al. 2019, *MNRAS*, 483, 3636, doi: [10.1093/mnras/sty3318](https://doi.org/10.1093/mnras/sty3318)
- Cox, D. P., & Reynolds, R. J. 1987, *ARA&A*, 25, 303, doi: [10.1146/annurev.aa.25.090187.001511](https://doi.org/10.1146/annurev.aa.25.090187.001511)
- Cukierman, A. J., Clark, S. E., & Halal, G. 2023, *ApJ*, 946, 106, doi: [10.3847/1538-4357/acb0c4](https://doi.org/10.3847/1538-4357/acb0c4)
- Cutri, R. M., Wright, E. L., Conrow, T., et al. 2013, Explanatory Supplement to the AllWISE Data Release Products, Explanatory Supplement to the AllWISE Data Release Products, by R. M. Cutri et al.
- Dawson, J. R. 2013, *PASA*, 30, e025, doi: [10.1017/pas.2013.002](https://doi.org/10.1017/pas.2013.002)
- Edenhofer, G., Zucker, C., Frank, P., et al. 2023, arXiv e-prints, arXiv:2308.01295, doi: [10.48550/arXiv.2308.01295](https://doi.org/10.48550/arXiv.2308.01295)
- Elmegreen, B. G. 2011, in *EAS Publications Series*, Vol. 51, *EAS Publications Series*, ed. C. Charbonnel & T. Montmerle, 45–58, doi: [10.1051/eas/1151004](https://doi.org/10.1051/eas/1151004)
- Enßlin, T. A. 2019, *Annalen der Physik*, 531, 1800127, doi: [10.1002/andp.201800127](https://doi.org/10.1002/andp.201800127)
- Farhang, A., van Loon, J. T., Khosroshahi, H. G., Javadi, A., & Bailey, M. 2019, *Nature Astronomy*, 3, 922, doi: [10.1038/s41550-019-0814-z](https://doi.org/10.1038/s41550-019-0814-z)
- Ferrière, K. M. 2001, *Reviews of Modern Physics*, 73, 1031, doi: [10.1103/RevModPhys.73.1031](https://doi.org/10.1103/RevModPhys.73.1031)
- Fiege, J. D., & Pudritz, R. E. 2000, *ApJ*, 544, 830, doi: [10.1086/317228](https://doi.org/10.1086/317228)
- Finkbeiner, D. P. 2003, *ApJS*, 146, 407, doi: [10.1086/374411](https://doi.org/10.1086/374411)
- Fitzpatrick, E. L., Massa, D., Gordon, K. D., Bohlin, R., & Clayton, G. C. 2019, *ApJ*, 886, 108, doi: [10.3847/1538-4357/ab4c3a](https://doi.org/10.3847/1538-4357/ab4c3a)
- Flewelling, H. A., Magnier, E. A., Chambers, K. C., et al. 2020, *ApJS*, 251, 7, doi: [10.3847/1538-4365/abb82d](https://doi.org/10.3847/1538-4365/abb82d)
- Frisch, P. C., Andersson, B. G., Berdyugin, A., et al. 2012, *ApJ*, 760, 106, doi: [10.1088/0004-637X/760/2/106](https://doi.org/10.1088/0004-637X/760/2/106)
- Frisch, P. C., Berdyugin, A., Piirola, V., et al. 2015, *ApJ*, 814, 112, doi: [10.1088/0004-637X/814/2/112](https://doi.org/10.1088/0004-637X/814/2/112)
- Gaia Collaboration, Brown, A. G. A., Vallenari, A., et al. 2018, *A&A*, 616, A1, doi: [10.1051/0004-6361/201833051](https://doi.org/10.1051/0004-6361/201833051)
- Gaia Collaboration, Vallenari, A., Brown, A. G. A., et al. 2023, *A&A*, 674, A1, doi: [10.1051/0004-6361/202243940](https://doi.org/10.1051/0004-6361/202243940)
- Gontcharov, G. A., & Mosenkov, A. V. 2019, *MNRAS*, 483, 299, doi: [10.1093/mnras/sty2978](https://doi.org/10.1093/mnras/sty2978)
- Górski, K. M., Hivon, E., Banday, A. J., et al. 2005, *ApJ*, 622, 759, doi: [10.1086/427976](https://doi.org/10.1086/427976)
- Green, G. M. 2018, *Journal of Open Source Software*, 3, 695, doi: [10.21105/joss.00695](https://doi.org/10.21105/joss.00695)
- Halal, G., Clark, S. E., Cukierman, A., Beck, D., & Kuo, C.-L. 2024, *ApJ*, 961, 29, doi: [10.3847/1538-4357/ad06aa](https://doi.org/10.3847/1538-4357/ad06aa)
- Heiles, C. 1997, *ApJS*, 111, 245, doi: [10.1086/313010](https://doi.org/10.1086/313010)
- Heiles, C., & Haverkorn, M. 2012, *SSRv*, 166, 293, doi: [10.1007/s11214-012-9866-4](https://doi.org/10.1007/s11214-012-9866-4)
- Hensley, B. S., Zhang, C., & Bock, J. J. 2019, *ApJ*, 887, 159, doi: [10.3847/1538-4357/ab5183](https://doi.org/10.3847/1538-4357/ab5183)
- Hunter, J. D. 2007, *Computing in Science and Engineering*, 9, 90, doi: [10.1109/MCSE.2007.55](https://doi.org/10.1109/MCSE.2007.55)
- Hutschenreuter, S., Haverkorn, M., Frank, P., Raycheva, N. C., & Enßlin, T. A. 2023, arXiv e-prints, arXiv:2304.12350, doi: [10.48550/arXiv.2304.12350](https://doi.org/10.48550/arXiv.2304.12350)
- Inutsuka, S.-i., Inoue, T., Iwasaki, K., & Hosokawa, T. 2015, *A&A*, 580, A49, doi: [10.1051/0004-6361/201425584](https://doi.org/10.1051/0004-6361/201425584)
- Kim, C.-G., & Ostriker, E. C. 2015, *ApJ*, 802, 99, doi: [10.1088/0004-637X/802/2/99](https://doi.org/10.1088/0004-637X/802/2/99)
- King, P. K., Chen, C.-Y., Fissel, L. M., & Li, Z.-Y. 2019, *MNRAS*, 490, 2760, doi: [10.1093/mnras/stz2628](https://doi.org/10.1093/mnras/stz2628)
- King, P. K., Fissel, L. M., Chen, C.-Y., & Li, Z.-Y. 2018, *MNRAS*, 474, 5122, doi: [10.1093/mnras/stx3096](https://doi.org/10.1093/mnras/stx3096)
- Kothes, R., & Brown, J.-A. 2009, in *Cosmic Magnetic Fields: From Planets, to Stars and Galaxies*, ed. K. G. Strassmeier, A. G. Kosovichev, & J. E. Beckman, Vol. 259, 75–80, doi: [10.1017/S1743921309030087](https://doi.org/10.1017/S1743921309030087)
- Krumholz, M. R., Stone, J. M., & Gardiner, T. A. 2007, *ApJ*, 671, 518, doi: [10.1086/522665](https://doi.org/10.1086/522665)
- Lallement, R., Babusiaux, C., Vergely, J. L., et al. 2019, *A&A*, 625, A135, doi: [10.1051/0004-6361/201834695](https://doi.org/10.1051/0004-6361/201834695)

- Lallement, R., Vergely, J. L., Valette, B., et al. 2014, *A&A*, 561, A91, doi: [10.1051/0004-6361/201322032](https://doi.org/10.1051/0004-6361/201322032)
- Lallement, R., Welsh, B. Y., Vergely, J. L., Crifo, F., & Sfeir, D. 2003, *A&A*, 411, 447, doi: [10.1051/0004-6361:20031214](https://doi.org/10.1051/0004-6361:20031214)
- Lee, H. M., & Draine, B. T. 1985, *ApJ*, 290, 211, doi: [10.1086/162974](https://doi.org/10.1086/162974)
- Lei, M., & Clark, S. E. 2023, arXiv e-prints, arXiv:2312.03846, doi: [10.48550/arXiv.2312.03846](https://doi.org/10.48550/arXiv.2312.03846)
- Leike, R. H., Glatzle, M., & Enßlin, T. A. 2020, *A&A*, 639, A138, doi: [10.1051/0004-6361/202038169](https://doi.org/10.1051/0004-6361/202038169)
- Lenz, D., Hensley, B. S., & Doré, O. 2017, *ApJ*, 846, 38, doi: [10.3847/1538-4357/aa84af](https://doi.org/10.3847/1538-4357/aa84af)
- Leroy, J. L. 1999, *A&A*, 346, 955
- Liu, W., Chiao, M., Collier, M. R., et al. 2017, *ApJ*, 834, 33, doi: [10.3847/1538-4357/834/1/33](https://doi.org/10.3847/1538-4357/834/1/33)
- Maíz-Apellániz, J. 2001, *ApJL*, 560, L83, doi: [10.1086/324016](https://doi.org/10.1086/324016)
- Manchester, R. N., Hobbs, G. B., Teoh, A., & Hobbs, M. 2005, *AJ*, 129, 1993, doi: [10.1086/428488](https://doi.org/10.1086/428488)
- Medan, I., & Andersson, B. G. 2019, *ApJ*, 873, 87, doi: [10.3847/1538-4357/ab063c](https://doi.org/10.3847/1538-4357/ab063c)
- Oliphant, T. E. 2015, *Guide to NumPy*, 2nd edn. (North Charleston, SC, USA: CreateSpace Independent Publishing Platform)
- O'Neill, T. J., Zucker, C., Goodman, A. A., & Edenhofer, G. 2024, arXiv e-prints, arXiv:2403.04961, doi: [10.48550/arXiv.2403.04961](https://doi.org/10.48550/arXiv.2403.04961)
- O'Neill, T., Goodman, A., Soler, J., Han, J. J., & Zucker, C. 2023, doi: [10.22541/au.167303779.92162611/v3](https://doi.org/10.22541/au.167303779.92162611/v3)
- Padoan, P., Goodman, A., Draine, B. T., et al. 2001, *ApJ*, 559, 1005, doi: [10.1086/322504](https://doi.org/10.1086/322504)
- Panopoulou, G. V., & Lenz, D. 2020, *ApJ*, 902, 120, doi: [10.3847/1538-4357/abb6f5](https://doi.org/10.3847/1538-4357/abb6f5)
- Panopoulou, G. V., Tassis, K., Skalidis, R., et al. 2019, *ApJ*, 872, 56, doi: [10.3847/1538-4357/aafdb2](https://doi.org/10.3847/1538-4357/aafdb2)
- Pattle, K., Fissel, L., Tahani, M., Liu, T., & Ntormousi, E. 2023, in *Astronomical Society of the Pacific Conference Series*, Vol. 534, *Protostars and Planets VII*, ed. S. Inutsuka, Y. Aikawa, T. Muto, K. Tomida, & M. Tamura, 193, doi: [10.48550/arXiv.2203.11179](https://doi.org/10.48550/arXiv.2203.11179)
- Pelgrims, V., Clark, S. E., Hensley, B. S., et al. 2021, *A&A*, 647, A16, doi: [10.1051/0004-6361/202040218](https://doi.org/10.1051/0004-6361/202040218)
- Pelgrims, V., Ferrière, K., Boulanger, F., Lallement, R., & Montier, L. 2020, *A&A*, 636, A17, doi: [10.1051/0004-6361/201937157](https://doi.org/10.1051/0004-6361/201937157)
- Pelkonen, V. M., Juvela, M., & Padoan, P. 2007, *A&A*, 461, 551, doi: [10.1051/0004-6361:20065838](https://doi.org/10.1051/0004-6361:20065838)
- Planck Collaboration, Abergel, A., Ade, P. A. R., et al. 2014, *A&A*, 571, A11, doi: [10.1051/0004-6361/201323195](https://doi.org/10.1051/0004-6361/201323195)
- Planck Collaboration, Aghanim, N., Ashdown, M., et al. 2016a, *A&A*, 596, A109, doi: [10.1051/0004-6361/201629022](https://doi.org/10.1051/0004-6361/201629022)
- Planck Collaboration, Adam, R., Ade, P. A. R., et al. 2016b, *A&A*, 594, A10, doi: [10.1051/0004-6361/201525967](https://doi.org/10.1051/0004-6361/201525967)
- Planck Collaboration, Aghanim, N., Akrami, Y., et al. 2020a, *A&A*, 641, A12, doi: [10.1051/0004-6361/201833885](https://doi.org/10.1051/0004-6361/201833885)
- . 2020b, *A&A*, 641, A1, doi: [10.1051/0004-6361/201833880](https://doi.org/10.1051/0004-6361/201833880)
- Plaszczynski, S., Montier, L., Levrier, F., & Tristram, M. 2014, *MNRAS*, 439, 4048, doi: [10.1093/mnras/stu270](https://doi.org/10.1093/mnras/stu270)
- Purcell, E. M. 1975, in *The Dusty Universe*, ed. G. B. Field & A. G. W. Cameron, 155–167
- Puspitarini, L., & Lallement, R. 2012, *A&A*, 545, A21, doi: [10.1051/0004-6361/201219284](https://doi.org/10.1051/0004-6361/201219284)
- Remazeilles, M., Delabrouille, J., & Cardoso, J.-F. 2011, *MNRAS*, 418, 467, doi: [10.1111/j.1365-2966.2011.19497.x](https://doi.org/10.1111/j.1365-2966.2011.19497.x)
- Rosolowsky, E. W., Pineda, J. E., Kauffmann, J., & Goodman, A. A. 2008, *ApJ*, 679, 1338, doi: [10.1086/587685](https://doi.org/10.1086/587685)
- Sandstrom, K. M., Koch, E. W., Leroy, A. K., et al. 2023, *ApJL*, 944, L8, doi: [10.3847/2041-8213/aca972](https://doi.org/10.3847/2041-8213/aca972)
- Santos, F. P., Corradi, W., & Reis, W. 2011, *ApJ*, 728, 104, doi: [10.1088/0004-637X/728/2/104](https://doi.org/10.1088/0004-637X/728/2/104)
- Sfeir, D. M., Lallement, R., Crifo, F., & Welsh, B. Y. 1999, *A&A*, 346, 785
- Skalidis, R., & Pelgrims, V. 2019, *A&A*, 631, L11, doi: [10.1051/0004-6361/201936547](https://doi.org/10.1051/0004-6361/201936547)
- Skrutskie, M. F., Cutri, R. M., Stiening, R., et al. 2006, *AJ*, 131, 1163, doi: [10.1086/498708](https://doi.org/10.1086/498708)
- Soler, J. D., Bracco, A., & Pon, A. 2018, *A&A*, 609, L3, doi: [10.1051/0004-6361/201732203](https://doi.org/10.1051/0004-6361/201732203)
- Sullivan, C. H., Fissel, L. M., King, P. K., et al. 2021, *MNRAS*, 503, 5006, doi: [10.1093/mnras/stab596](https://doi.org/10.1093/mnras/stab596)
- Tahani, M., Plume, R., Brown, J. C., & Kainulainen, J. 2018, *A&A*, 614, A100, doi: [10.1051/0004-6361/201732219](https://doi.org/10.1051/0004-6361/201732219)
- Tahani, M., Glover, J., Lupypciw, W., et al. 2022a, *A&A*, 660, L7, doi: [10.1051/0004-6361/202243322](https://doi.org/10.1051/0004-6361/202243322)
- Tahani, M., Lupypciw, W., Glover, J., et al. 2022b, *A&A*, 660, A97, doi: [10.1051/0004-6361/202141170](https://doi.org/10.1051/0004-6361/202141170)
- Tahani, M., Bastien, P., Furuya, R. S., et al. 2023, *ApJ*, 944, 139, doi: [10.3847/1538-4357/acac81](https://doi.org/10.3847/1538-4357/acac81)
- Tassis, K., & Pavlidou, V. 2015, *MNRAS*, 451, L90, doi: [10.1093/mnrasl/slv077](https://doi.org/10.1093/mnrasl/slv077)
- Tassis, K., Ramaprakash, A. N., Readhead, A. C. S., et al. 2018, arXiv e-prints, arXiv:1810.05652, doi: [10.48550/arXiv.1810.05652](https://doi.org/10.48550/arXiv.1810.05652)

- Van Eck, C. L., Haverkorn, M., Alves, M. I. R., et al. 2017, *A&A*, 597, A98, doi: [10.1051/0004-6361/201629707](https://doi.org/10.1051/0004-6361/201629707)
- Van Eck, C. L., Gaensler, B. M., Hutschenreuter, S., et al. 2023, *ApJS*, 267, 28, doi: [10.3847/1538-4365/acda24](https://doi.org/10.3847/1538-4365/acda24)
- Vergely, J. L., Lallement, R., & Cox, N. L. J. 2022, *A&A*, 664, A174, doi: [10.1051/0004-6361/202243319](https://doi.org/10.1051/0004-6361/202243319)
- Virtanen, P., Gommers, R., Oliphant, T. E., et al. 2020, *Nature Methods*, 17, 261, doi: [10.1038/s41592-019-0686-2](https://doi.org/10.1038/s41592-019-0686-2)
- Watkins, E. J., Barnes, A. T., Henny, K., et al. 2023, *ApJL*, 944, L24, doi: [10.3847/2041-8213/aca6e4](https://doi.org/10.3847/2041-8213/aca6e4)
- Welsh, B. Y. 1991, *ApJ*, 373, 556, doi: [10.1086/170074](https://doi.org/10.1086/170074)
- Welsh, B. Y., Sallmen, S., & Lallement, R. 2004, *A&A*, 414, 261, doi: [10.1051/0004-6361:20034367](https://doi.org/10.1051/0004-6361:20034367)
- Zhang, X., Green, G. M., & Rix, H.-W. 2023, *MNRAS*, 524, 1855, doi: [10.1093/mnras/stad1941](https://doi.org/10.1093/mnras/stad1941)
- Zonca, A., Singer, L., Lenz, D., et al. 2019, *The Journal of Open Source Software*, 4, 1298, doi: [10.21105/joss.01298](https://doi.org/10.21105/joss.01298)
- Zucker, C., Goodman, A., Alves, J., et al. 2021, *ApJ*, 919, 35, doi: [10.3847/1538-4357/ac1f96](https://doi.org/10.3847/1538-4357/ac1f96)
- Zucker, C., Goodman, A. A., Alves, J., et al. 2022, *Nature*, 601, 334, doi: [10.1038/s41586-021-04286-5](https://doi.org/10.1038/s41586-021-04286-5)